

## Article

# The Influence of La and Ce on Microstructure and Mechanical Properties of an Al-Si-Cu-Mg-Fe Alloy at High Temperature

Andong Du<sup>1,2</sup>, Anders E. W. Jarfors<sup>1,3,\*</sup> , Jinchuan Zheng<sup>1</sup>, Kaikun Wang<sup>2</sup> and Gegang Yu<sup>1</sup>

<sup>1</sup> China Academy of Machinery Sciences and Technology (Jiangle), Institute of Semi-solid Metal Technology, Sanming 353300, China; b20170186@xs.ustb.edu.cn (A.D.); zhengjc@cam.com.cn (J.Z.); yugg@cam.com.cn (G.Y.)

<sup>2</sup> School of Materials Science and Engineering, University of Science and Technology Beijing, Beijing 100083, China; kkwang@mater.ustb.edu.cn

<sup>3</sup> School of Engineering, Department of Materials and Manufacturing, Jönköping University, 55111 Jönköping, Sweden

\* Correspondence: anders.jarfors@ju.se; Tel.: +46-(0)722392889

**Abstract:** The effect of lanthanum (La)+cerium (Ce) addition on the high-temperature strength of an aluminum (Al)–silicon (Si)–copper (Cu)–magnesium (Mg)–iron (Fe)–manganese (Mn) alloy was investigated. A great number of plate-like intermetallics, Al<sub>11</sub>(Ce, La)<sub>3</sub>- and blocky α-Al<sub>15</sub>(Fe, Mn)<sub>3</sub>Si<sub>2</sub>-precipitates, were observed. The results showed that the high-temperature mechanical properties depended strongly on the amount and morphology of the intermetallic phases formed. The precipitated tiny Al<sub>11</sub>(Ce, La)<sub>3</sub> and α-Al<sub>15</sub>(Fe, Mn)<sub>3</sub>Si<sub>2</sub> both contributed to the high-temperature mechanical properties, especially at 300 °C and 400 °C. The formation of coarse plate-like Al<sub>11</sub>(Ce, La)<sub>3</sub>, at the highest (Ce-La) additions, reduced the mechanical properties at (≤300) °C and improved the properties at 400 °C. Analysis of the strengthening mechanisms revealed that the load-bearing mechanism was the main contributing mechanism with no contribution from thermal-expansion mismatch effects. Strain hardening had a minor contribution to the tensile strength at high-temperature.

**Keywords:** Ce+La; Al<sub>11</sub>La<sub>3</sub>/Al<sub>11</sub>Ce<sub>3</sub>; high-temperature strength; modeling particle contribution



**Citation:** Du, A.; Jarfors, A.E.W.; Zheng, J.; Wang, K.; Yu, G. The Influence of La and Ce on Microstructure and Mechanical Properties of an Al-Si-Cu-Mg-Fe Alloy at High Temperature. *Metals* **2021**, *11*, 384. <https://doi.org/10.3390/met11030384>

Academic Editor: Martin Heilmaier

Received: 18 December 2020

Accepted: 21 February 2021

Published: 26 February 2021

**Publisher's Note:** MDPI stays neutral with regard to jurisdictional claims in published maps and institutional affiliations.



**Copyright:** © 2021 by the authors. Licensee MDPI, Basel, Switzerland. This article is an open access article distributed under the terms and conditions of the Creative Commons Attribution (CC BY) license (<https://creativecommons.org/licenses/by/4.0/>).

## 1. Introduction

The growing focus on reducing greenhouse gas emissions and the associated needs of reduction of energy usage makes energy efficiency a prioritized matter [1]. The transport sector is responsible for more than one-quarter of the total CO<sub>2</sub> emissions. One possible route to reduce the CO<sub>2</sub> emissions is by weight reduction of the vehicles used for transportation and effectively increase the payload to vehicle ratio. The weight reduction has been reported to possibly be even more important than electrification before 2050, as it today is a significant amount of electricity produced using fossil fuels, resulting in significant CO<sub>2</sub> emissions [2]. In the strive for weight reduction, the greatest gains can be made on the moving parts as they add to inertia during acceleration. The brake disk rotor is such a component and is today usually made from cast iron [3]. A material change from cast iron to an Al-based metal matrix composite (Al-MMC) material could result in a 47% weight reduction, as well as a decrease of the inertia during acceleration and braking. However, this material change is very challenging as the cast-iron brake disk rotor may be subjected to a high thermal load, which results in a sudden local increase of temperature up to as high as 700 °C. This is not possible for an Al-based disk rotor. The brake disk rotor usage in electric vehicles will reduce the need for extreme temperature performance. However, the local temperature increase may still be high at the brake pad contact, resulting in significant softening of the aluminum base. Nowadays, improved high-temperature mechanical properties of a composite matrix have become an important research area, also for Al-MMCs and is an emerging brake disk rotor material [4].

Al-based composite brake disc could be the future choice of the automotive industry. It would reduce vehicle emissions and improve particle emissions and improve the brake disc's esthetics by improved corrosion resistance and reduced staining [3]. Hard phases such as SiC/Cr particulates can increase friction and surface hardness, making them ideal for brake rotor applications [4]. The maximum service temperature limitations are found at the Al-based material leading to a direct need for improved high-temperature performance of the Al-matrix material in the Al-MMC material [5].

The conventional strengthening mechanisms used in alloy design include (i) grain boundary strengthening, (ii) precipitation hardening, (iii) solution hardening, (iv) deformation hardening (v) Peierls–Nabarro hardening [6].

In addition to the conventional mechanisms used in alloying, the formation of large thermally stable phases may contribute to the aluminum matrix similarly to the composite reinforcement (SiC, Al<sub>2</sub>O<sub>3</sub>). The main additional strengthening mechanisms in composite materials are (i) load-bearing strengthening, (ii) thermal expansion mismatch strengthening, and (iii) modulus mismatch strengthening. It should be noted that the modulus mismatch effect is similar to that of deformation hardening and will not for a cast material contribute to the yield point but will affect the strain hardening of a material [7].

Several criteria need to be fulfilled to contribute to strengthening the effort to develop aluminum alloys with superior high-temperature strength. The main contribution should come from particles, and thus it is essential that the alloying elements (i) form a thermally stable strengthening phase and that any changes to the particles are sluggish (ii) low solubility in Al alloy (iii) low diffusivity in Al alloy [8]. The transition metals Mn, zirconium (Zr), molybdenum (Mo), titanium (Ti) have low solubility in Al alloy, and all could form thermal strengthening precipitates [9]. The currently existing alloys for specific elevated temperature use and their properties are collated in Table 1. From Table 1, it is evident that the existing commercial Al-alloys perform reasonably up to 200 °C. Between 200 and 300 °C, there is a significant drop in strength for most alloys. The alloys with the highest performance (A319, 332 and 354) all contain Cu as an alloying element. Cu is eco-toxic and not an ideal alloying element in the application that could release debris into nature due to the oxidative stress on living organisms [10]. As such, it is of interest to keep Cu contents low in the alloy. Cu additions do, however, rely on slow diffusion to maintain properties at elevated temperatures. Still, this mechanism fails at temperatures above 350 °C which would be a requirement for brake discs.

The main common larger phase existing in cast alloys are the Fe-bearing intermetallics. Shaha et al. [8] showed that minor additions of Mn significantly alter the cast Al-7Si-1Cu-0.5Mg alloy with an increase of both Ultimate Tensile Strength (UTS) and ductility compared to the base alloy without Mn additions. Mn changes the Fe intermetallics morphology and allows them to contribute to strength instead of being detrimental. At room temperature, the contribution to strength may be in the order of 12 MPa, primarily through load-bearing effects [11].

In Table 1, examples of high-temperature properties of new alloys are also shown. Usually, the alloying elements nickel (Ni), Cu, Mg have been used to improve the high-temperature properties of Al alloy by various strengthening mechanisms, such as grain refinement, solution hardening. These strengthening methods will be affected at elevated temperatures [12]. Furthermore, the rare earth element (RE) additions could form stable thermal phases, which could improve the Al alloy's high-temperature strength. These particles will be incoherent, which is in contrast with the conventional particles formed during precipitation hardening that would be coherent [13].

Bogdanoff et al. [14] showed that the combined addition of cobalt (Co) and Ni improved the mechanical properties of a cast Al-Si alloy at elevated temperatures with a 32% improvement of UTS at 230 °C, this improvement could be a result of dispersion strengthening or due to higher degree of contiguity in the 3D network of Co- and Ni-rich phases and eutectic Al-Si. Florian et al. [15] investigated the effect of Ni on the high-temperature strength of Al-Si cast alloys; the strength can be increased at 250 °C, Al<sub>3</sub>Ni phases stabilized

the Al-Si eutectic network. Feng et al. [16] also studied the effect of Ni and concluded that  $\epsilon$ -Al<sub>3</sub>Ni improves the Al-12Si-0.9Cu-0.8Mg-xNi tensile strength and is thermally stable at 350 °C, the UTS improved from 94 Mpa to 116 Mpa with the Ni additions increasing from 1% up to 4%.

Song et al. [17] reported that the Ce addition could improve the nucleation of the  $\Omega$ -phase (Al<sub>2</sub>Cu) then decrease the diffusivity of the Cu atoms, thus improve the Al-Cu-Mg-Ag alloy strength at both room and elevated temperature, and this would improve precipitation hardening. However, the work by Song et al. [17] does indicate that RE addition may affect diffusivity of at least Cu and thus aid large particle stability. Liao et al. [18] added 0.5% (Ce + La) to an Al-12% Si-4% Cu-1.6% Mn alloy, then the strength at 200 and 300 °C increased by 2.3% and 6%, respectively.

**Table 1.** Conventional Al alloys and their high-temperature performance.

Al Alloys	UTS T > 100 °C	UTS T > 200 °C	UTS T > 250 °C	UTS T > 300 °C	UTS T > 350 °C	Ref.
A319		225 MPa/200 °C		90.8 MPa/300 °C	25.6 MPa/400 °C	[19]
360		150 MPa/205 °C		50 MPa/315 °C	30 MPa/370 °C	[20]
A360		145 MPa/205 °C		45 MPa/315 °C	30 MPa/370 °C	[20]
359		125 MPa/260 °C		50 MPa/315 °C	30 MPa/370 °C	[21]
319		140 MPa/200 °C		66 MPa/315 °C	48 MPa/370 °C	[22]
332		165 MPa/205 °C	110 MPa/260 °C	90 MPa/315 °C		[23]
354	325 MPa/150 °C	290 MPa/205 °C		90 MPa/315 °C		[24]
355/T5	160 MPa/150 °C	103 MPa/205 °C			25 MPa/371 °C	[25]
356/T6		83 MPa/205 °C		28 MPa/315 °C	17 MPa/375 °C	[26]
A357/T62	270 MPa/150 °C	250 MPa/205 °C		70 MPa/315 °C		[27]
EN-AC46000		215 MPa/200 °C		110 MPa/300 °C	20 MPa/400 °C	[28]

The RE elements used in aluminum alloys usually refine the microstructure to improve the room temperature tensile properties through grain boundary strengthening [29]. At the same time, the effect of RE additions on the high-temperature properties of aluminum alloys has not been investigated in any great detail. The current study aims to examine the effect of RE element (Ce and La) additions on the mechanical properties at both room temperature and high temperature. The Al-alloy investigated were experimental Al-based alloys derived from EN-AC 46000, adapted for squeeze casting and elevated temperature use, with room temperature strength suitable for a brake disc application. The alloying elements considered were Cu, Ni, Mg, Si added with Ce and La. A special adaptation consisted of a lower Cu-content for reduced eco-toxicity and an increased Ni content to promote high-temperature strength. Mn is kept high to support solution hardening that is an effect with a smaller temperature sensitivity than those involving precipitation and particles [8]. Mn is also added to control the Fe-intermetallics morphology.

## 2. Experimental

### 2.1. Sample Manufacturing

#### 2.1.1. Alloy Fabrication

Four different alloys were tested with compositions (by weight) collated in Table 2. The EN-AC46000 alloy is included as a baseline reference. The EN-AC46000 alloy is commonly used for cylinder heads and pistons of engines. Due to the eco-toxicity of Cu, a reduce the Cu-content was targeted to compensate for the loss of strengths through the (La + Ce) and Ni additions.

An electrical resistance crucible furnace, with 10 kg capacity, was used for alloy fabrication. The Al, Si, and Mg were of 99.98% purity. The master alloys consisted of Al-10% Ni, Al-30% Ce, Al-30% La, Al-50% Cu, Al-10% Ti, Al-20% Mn.

The Al and all master alloys were charged into the furnace. The Al-30% Ce- and Al-30% La-master alloys were placed at the bottom of the furnace and covered with pure Al alloy to minimize oxidation of the Ce and La elements. After reaching the preset

temperature of 800 °C, the melt was stirred by a graphite rod for 20 s every 5 minutes until all the master alloys were fully dissolved. Subsequently, Si was added, and the melt was stirred 10 s every 3 minutes until all Si dissolved. Before casting, the melt temperature was reduced to 750 °C, and dross was removed. The final addition of Mg was made before casting under argon protection to minimize oxidation losses. The compositions of the alloys, listed in Table 2, were measured using direct current plasma emission spectroscopy (DCPMS) (ATI Wah Chang, Albany, OR, USA). Please note that due to analysis limitations Ce and La could not be assessed using DCPMS, and Ce and La are given as nominal values by addition.

**Table 2.** Chemical composition (wt %) of the 4 alloys used in the present study.

Alloy No.	EN AC 46000	A1	A2	A3	A4	Comment
Element	(wt)%	(wt)%	(wt)%	(wt)%	(wt)%	
Copper (Cu)	2–4	1.84	1.82	1.92	1.84	Ecotoxicity
Nickel (Ni)	<0.55	1.74	1.76	1.87	1.73	Elevated temperature performance
Iron (Fe)	0.6–1.1	0.15	0.14	0.14	0.10	Kept low for ductility
Manganese (Mn)	<0.55	0.86	0.89	0.76	0.74	Solution hardening
Titanium (Ti)	0.2	0.14	0.19	0.14	0.25	Grain refinement
Magnesium (Mg)	0.15–0.55	0.80	0.88	0.86	0.91	Wetting agent for SiC additions
Silicon (Si)	8–11	10.00	9.88	10.20	9.50	Castability and hardness
Cerium (Ce)	0	0	0.5	1	2	Target for study
Lanthanum (La)	-	0	0.5	1	2	Target for study
Zinc (Zn)	<1.2	-	-	-	-	
Chromium (Cr)	<0.15	-	-	-	-	
Aluminum (Al)	Bal.	Bal.	Bal.	Bal.	Bal.	

### 2.1.2. Sample Casting

The casting was made at 700 °C using a squeeze casting process consisting of a 10 T hydraulic press with steel mold preheated to 180 °C. Figure 1 shows the steel mold and sample image. The sample was machined into a dog bone shape.

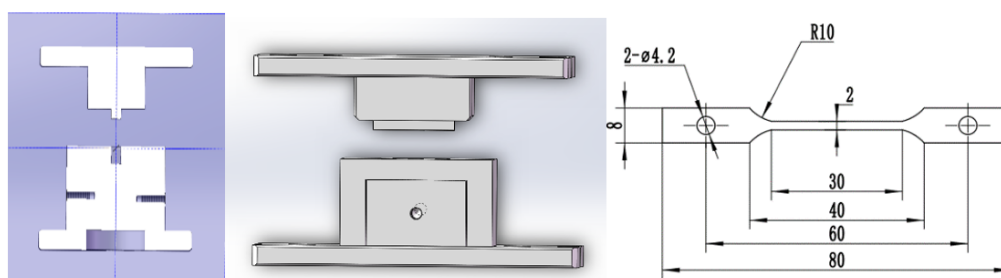


**Figure 1.** The die mold and tensile bar (All measures are shown in mm).

### 2.1.3. Sample Quality Assurance

Industrial X-ray inspection equipment (UNC225CT, UNICOMP, Guangdong, China) was used to detect sample defects. The voltage is set to 150 KV, and the electric current is set to 0.25 mA, which made the image clear. Porosity and oxide inclusion were detected; usually, porosity is seen as white dots on the photo; the oxide inclusion exhibit black dots.

## 2.2. Material Characterization

### 2.2.1. X-ray Diffraction Analysis

To identify the phase components occurring in the alloy, X-ray diffraction (XRD) analysis was performed with  $2\theta = 20^\circ$ – $90^\circ$  and a scanning step of  $0.02^\circ$ /step (model PW 1729, Philips, Amsterdam, Netherlands, with Co-K $\alpha$  radiation).

### 2.2.2. Scanning Electron Microscopy

Alloy microstructure was examined in a scanning electron microscope (FEI Quanta 250, FEI, Hillsboro, OR, USA) equipped with energy-dispersive spectroscopy (EDS; Oxford, UK) to establish the chemical composition and morphology of the phases precipitated. Standard metallographic preparation procedures were used. To reveal the microstructure, the samples were etched, using Keller's reagent for 5 s. The size and fraction of the precipitated particles were measured using the Image-J image analysis software (by edge finding). Similarly, the secondary dendrite arm spacing (SDAS) was used to establish effects similar to the grain boundary strengthening effects in a cast microstructure where SDAS is more physically relevant for Al-alloys than actual grain size [30].

### 2.2.3. Hardness

The hardness tests were carried out at room temperature using a spherical indenter (tempered steel) with a diameter of 2.5 mm and a load of 62.5 kgf (HBE-3000A). The hardness of each alloy was obtained as an average value of five measurements. The hardness was measured following the principle GB/T 231.2 standard [31].

### 2.2.4. Tensile Tests at Room and Elevated Temperatures

Three samples were tested at each test temperature to obtain tensile results based on ASTM E8. The tensile properties of the alloys at the temperature (25 °C, 200 °C, 300 °C, and 400 °C) were evaluated in a universal material testing machine (Instron 1185) at a nominal strain rate of  $10^{-3} \text{ s}^{-1}$ .

## 3. Results and Discussion

### 3.1. Internal Soundness of the Test Material

The sample internal soundness was established using X-ray analysis, Figure 2. The castings were deemed as sound in the absence of visible porosity. There are some shadows visible, but the nature of these shadows could not be verified as oxides or other possible defects.

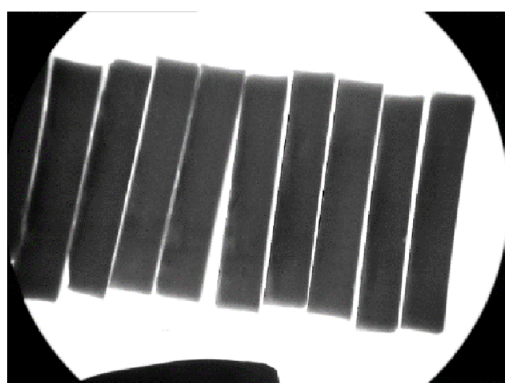
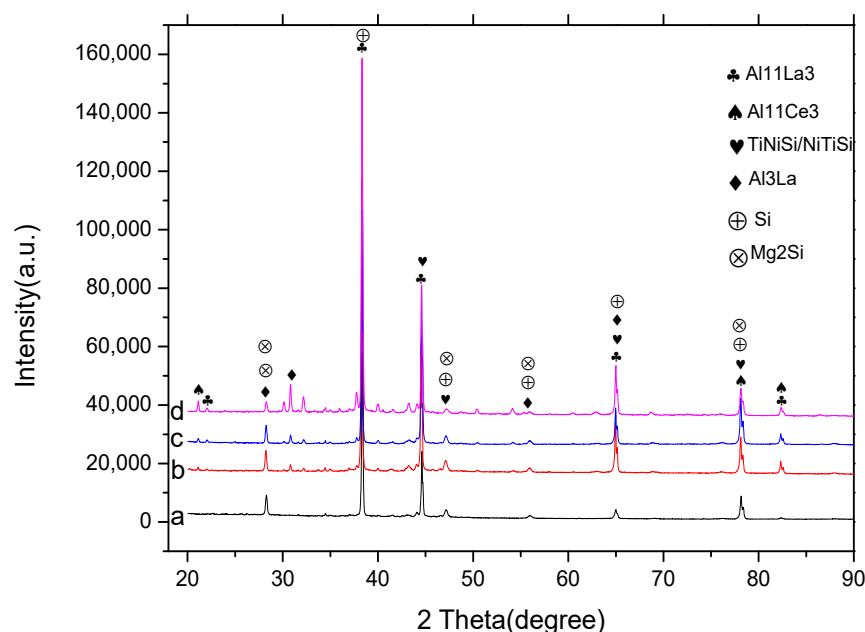


Figure 2. X-ray image showing no significant presence of porosity.

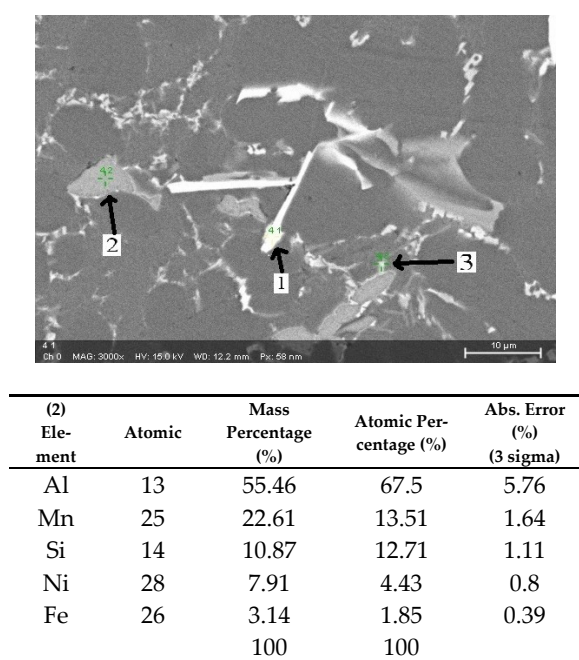
### 3.2. Microstructural Characteristics

The results from the XRD analysis are shown in Figure 3. Ce and La's addition changes the peaks present, but the actual determination is difficult due to many overlaps. The baseline Figure 3a is the XRD spectrum for the alloy without Ce and La additions providing the lines for Si and  $\text{Mg}_2\text{Si}$ . The addition of Ce and La adds new lines near  $20^\circ$ ,  $30^\circ$ , and just below  $80^\circ$ . These lines are associated with  $\text{Al}_{11}\text{Ce}_3$ ,  $\text{Al}_{11}\text{La}_3$ , and  $\text{Al}_3\text{La}$ . It should be noted that  $\text{Al}_{11}\text{Ce}_3$  (Pearson's symbol oI28) has the same crystallography as  $\text{Al}_{11}\text{La}_3$ , meaning that they are isomorphous and should be regarded as  $\text{Al}_{11}(\text{Ce}, \text{La})_3$ . The relative height of the peaks where these phases overlap Si and  $\text{Mg}_2\text{Si}$  are affected. In addition to this, weak evidence of the formation of NiTiSi was found [32].



**Figure 3.** XRD result of the 4 alloys where the lines indicated are (a) 0% (Ce + La), (b) 1% (Ce + La), (c) 2% (Ce + La) and, (d) 4% (Ce + La).

An example of the 1% (Ce + La) sample is shown in Figure 4. The size of the precipitate made an accurate analysis of the composition of the particle difficult. The bright phase marked as (1) in Figure 4 contains Ce, La, and Ni in contrast to the other phases in the image. This suggests that it is the  $\text{Al}_{11}(\text{Ce, La})_3$  phase. Interesting to note is also that Cu appears to dissolve into the phase. This suggests that  $\text{Al}_{11}(\text{Ce, La})_3$  precipitates as a plate. The second point marked (2) in Figure 4 shows the presence of Fe and Mn and Si suggesting that this is a Fe intermetallic with some dissolved Mn. From the literature [33,34], it was reported that Ce could modify the morphology of the  $\alpha\text{-Al}_{15}(\text{Fe, Mn})_3\text{Si}_2$  phase from large Chinese script-like into small and discrete blocky shape particles. No well-developed Chinese script-like particles could be found in the current study, suggesting that a similar modification occurred in the current study. Point (3) in Figure 4 is inconclusive.



(3) element	Atomic	Mass Percentage (%)	Atomic Percentage (%)	Abs. Error (%) (3 sigma)
Al	13	69.84	79.44	10.07
Ni	28	14.72	7.7	1.66
Si	14	6.51	7.12	0.96
Cu	29	5.16	2.71	0.87
Mg	12	1.69	2.13	0.38
Mn	25	1.64	0.91	0.32
		100	100	

**Figure 4.** SEM image and EDS analysis results for the 1% (Ce + La) sample.

The element mapping, Figure 5, displays a bright white plate-like phase that coincides with the Ce and La distribution, suggesting that it is Ce and La containing. The EDS analysis, Figure 4 of this white plate-like phase, shows that it is an aluminum-rich phase with an equiatomic contribution from Ce and La. Together with the XRD results, Figure 3, where the phase  $\text{Al}_{11}(\text{Ce, La})_3$  was confirmed, it can be concluded that the plate-like phase is  $\text{Al}_{11}(\text{Ce, La})_3$ . It can also be seen that the Ni distribution partially coincides with the Ce and La distribution, supporting the EDS measurements that presence for Ni in the  $\text{Al}_{11}(\text{Ce, La})_3$  plates was a correct interpretation and not an artifact, thus Ni is suggested to dissolve into  $\text{Al}_{11}(\text{Ce, La})_3$ .

The  $\alpha\text{-Al}_{15}(\text{Fe, Mn})_3\text{Si}_2$ , appearing as a blocky particle in Figure 4, may also turn up in different morphologies, Figure 5, where plate-like structures are found to contain Mn and Fe. No clear evidence of Ce nor La could be seen in the Fe and Mn-rich particle in Figure 5, but Figure 4 number 2 shows that the phase morphology is blocky and not the typical Chinese script morphology. It should be noted that Mg was not found in the  $\alpha\text{-Al}_{15}(\text{Fe, Mn})_3\text{Si}_2$  intermetallics, neither in the EDS analysis, Figure 4, nor in the EDS mapping, Figure 5. The absence of Mg dissolved in  $\alpha\text{-Al}_{15}(\text{Fe, Mn})_3\text{Si}_2$  excludes this phase from being the  $\pi\text{-Al}_8\text{Mg}_3\text{FeSi}_6$  phase. This is giving further evidence that the blocky phase was  $\alpha\text{-Al}_{15}(\text{Fe, Mn})_3\text{Si}_2$ , as it should contain 75 at-% Al, and the EDS analysis was 67 at-%, which is reasonable given the size and large uncertainty of the analysis. Si, Ni, Mg, and Cu are also enriched into the eutectic regions, Figure 5, suggesting possible precipitation of Si,  $\theta\text{-Al}_2\text{Cu}$ , and  $\text{Mg}_2\text{Si}$ . No clear and obvious evidence of the NiTiSi phase was found besides the overlapping peaks in the XRD analysis.

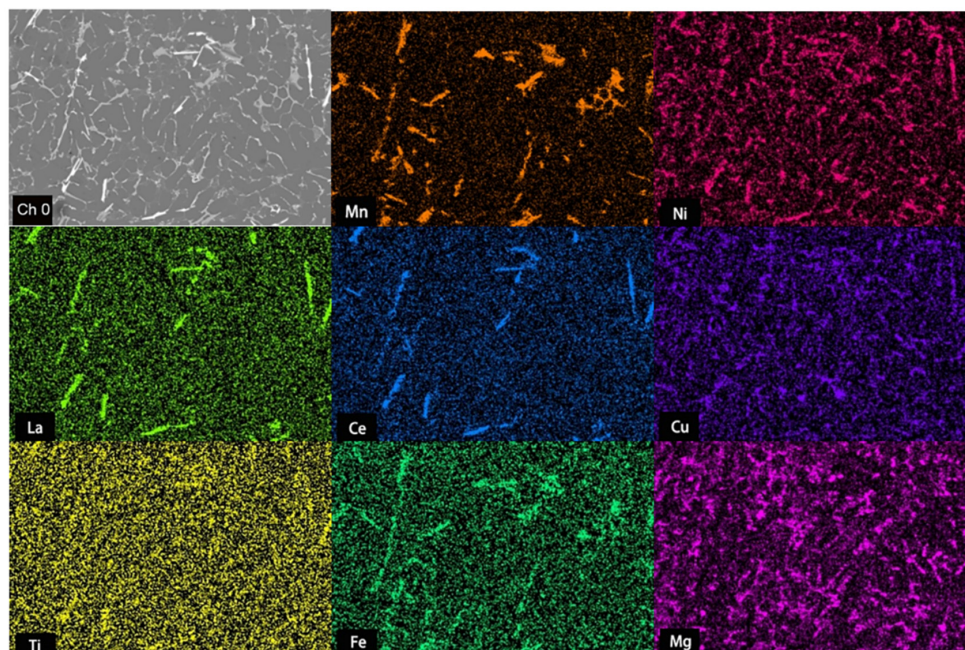
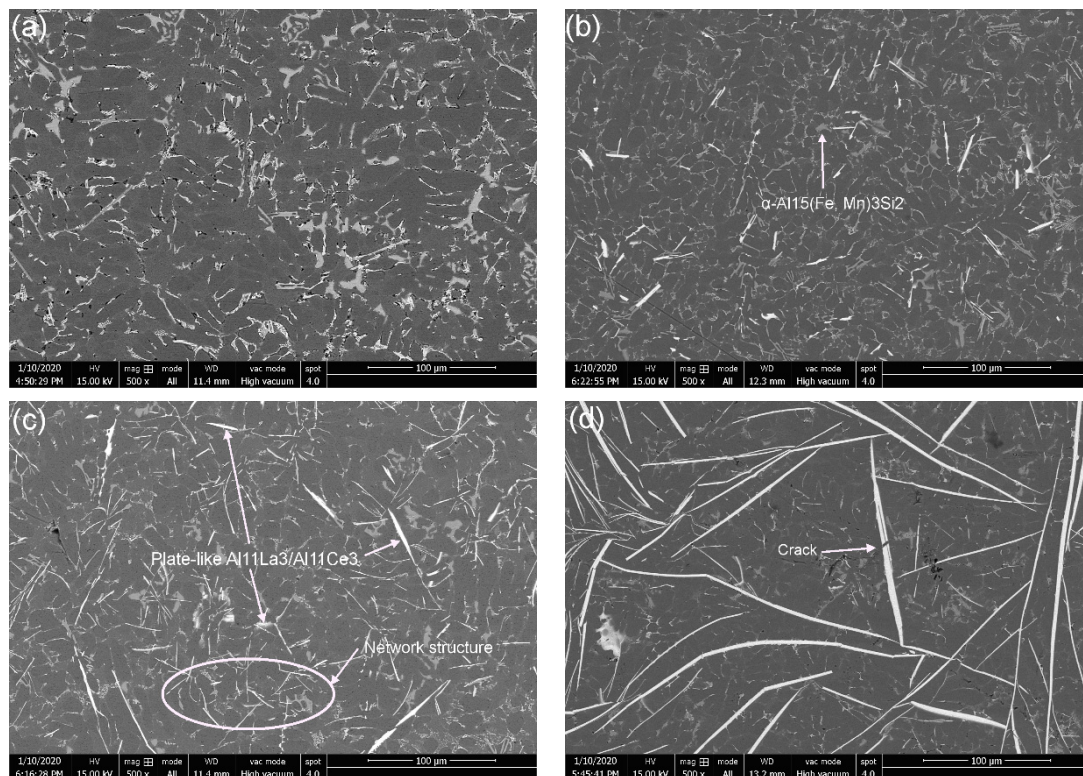


Figure 5. EDS element mapping for the 1% (Ce + La) sample.

Figure 6 shows the microstructures of the squeeze cast material for the different levels of (Ce and La) additions. Figure 6a is the base material showing a typical dendritic microstructure separated by eutectic regions. The addition of (Ce and La) results in the formation of additional phases that are primarily plate-like ( $\text{Al}_{11}(\text{Ce, La})_3$ ). Figure 6b shows that these plates are in the range of 10–40  $\mu\text{m}$  and found in the eutectic regions. This indicates that they are formed after the primary precipitating dendrites. In Figure 6b,  $\alpha\text{-Al}_{15}(\text{Fe, Mn})_3\text{Si}_2$  is found, indicating that the Mn additions were effective. Increasing the (Ce and La) content results in a size increase of the plates and the formation of a more interconnected network of these plates, Figure 6c. In Figure 6c, some larger plates may have precipitated as a primary phase as the Al dendrites seemingly have grown around

them and therefore came after in the precipitation sequence. Increasing the (Ce and La) additions further resulted in primary precipitation of large plates that reached lengths of 300  $\mu\text{m}$  and widths of 20  $\mu\text{m}$ . The tendency to form a network of  $\text{Al}_{11}(\text{Ce}, \text{La})_3$  also appears to be less as the smaller  $\text{Al}_{11}(\text{Ce}, \text{La})_3$  plates appears to be lesser, with the formation of the large primary precipitated  $\text{Al}_{11}(\text{Ce}, \text{La})_3$  plates, Figure 6d. While according to the report, the addition of combined (Ce and La) did not modify the A356 silicon morphology, even increase the coarseness of silicon particles [35].



**Figure 6.** SEM micrographs of the 4 alloy produced with (a) 0% (Ce + La), (b) 1% (Ce + La), (c) 2% (Ce + La) and, (d) 4% (Ce + La). The white plate-like particles are  $\text{Al}_{11}(\text{Ce}, \text{La})_3$ , blocky gray particles are  $\alpha\text{-Al}_{15}(\text{Fe}, \text{Mn})_3\text{Si}_2$ , gray non blocky regions are Al-Si eutectic.

The quantitative microstructural characterization is collected in Table 3. The first measure is the secondary dendrite arm spacing (SDAS), which was essentially unaltered by the addition of Ce and La. This will also result in that the Hall–Petch contribution from the matrix will be constant and approximately similar to that of the base alloy. The secondary particle size and fraction increased with increasing additions, which was also expected. These data will later be used for the modeling of the impact of the phases on the strength. The size measurement was made according to the Feret diameter principle. Regarding the addition of Ce and La, it can be concluded that the amounts in the  $\text{Al}_{11}(\text{Ce}, \text{La})_3$  phase were 15.25% Ce and 15.94% La (Figure 4). The resulting amounts added and bonded in particles can be estimated using the precipitated fractions, as collated in Table 3. This is a lower bound estimate on the effective amounts of the additions of Ce and La, neglecting the amounts dissolved in the matrix.

**Table 3.** Microstructural scales and fractions of intermetallics.

Alloy	A1	A2	A3	A4
SDAS ( $\mu\text{m}$ )	$27.31 \pm 0.72$	$28.80 \pm 3.10$	$32.00 \pm 5.71$	$26.28 \pm 4.09$
Particle Feret diameter ( $\mu\text{m}$ )	-	$14.35 \pm 7.13$	$19.70 \pm 12.37$	$40.62 \pm 31.38$
Particle fraction (%)	0	0.65	3.12	7.23
Ce weight percentage in particles (%)	0	0.09	0.48	1.15
La weight percentage in particles (%)	0	0.10	0.50	1.15

### 3.3. Mechanical Properties Characteristics

The results from the mechanical properties characterization are collated in Table 4.

**Table 4.** Room and high-temperature tensile test results with a comparison to EN AC-46000.

Alloys	RT	Yield Strength/YS (MPa)			Hardness HB
		200 °C	300 °C	400 °C	
A1	196	161	59	19.	70
A2	196.	154	69	28	70
A3	178	150	74	33	66
A4	104	103	78	41	68
Alloys	RT	Tensile Properties/UTS (MPa)			[27]
		200 °C	300 °C	400 °C	
EN AC 46000	280	215	110	20	[27]
A1	255	250	75	23	
A2	237	253	87	33	
A3	178	210	115	33	
A4	104	103	93	48	
Alloys	RT	Elongations/ $\epsilon$ (m/m)			
		200 °C	300 °C	400 °C	
A1	0.00940	0.02830	0.07890	0.13690	
A2	0.01090	0.01580	0.05120	0.22820	
A3	0.00630	0.01140	0.02010	0.14500	
A4	0.01500	0.00130	0.00830	0.04650	

#### 3.3.1. Hardness

Table 4 shows the hardness variation with RE addition. The addition of (Ce and La) had no significant influence on the hardness of the material despite that the particle fraction was increased. The precipitation sequence changed with the  $\text{Al}_{11}(\text{Ce}, \text{La})_3$  as primary precipitation the amount of eutectic appear to change with a weak reflection in the hardness, first, a weak softening followed by an increase with the appearance of large primary precipitates, Figure 6c,d, respectively.

#### 3.3.2. Tensile Properties

The tensile properties were studied in a temperature range of interest for application as brake disc rotors (25 °C, 200 °C, 300 °C, 400 °C). With the addition of elements that form larger secondary phases, room temperature properties typically reduce, and this was also the case in the current study

Figure 7 shows tensile strength and the effect of (Ce and La) additions at different temperatures. With a 4% (Ce and La) addition, a maximum reduction of more than 59% percent strength (from 254.81 MPa to 104.03 MPa) at room temperature. The increase of primary precipitated large coarse  $\text{Al}_{11}(\text{Ce}, \text{La})_3$  resulted in Figure 6d plates from the addition of 4% (Ce and La) shows brittle behavior. There is a crack in the coarse phases, which most likely formed during the squeeze casting process. This argument was further supported by the presence of bent particles on the left-hand side in Figure 6d. The presence

of cracks will, together with the stress concentration arising from the high aspect ratio plate-like primary precipitation of  $\text{Al}_{11}(\text{Ce, La})_3$ , result in a more brittle material [36].

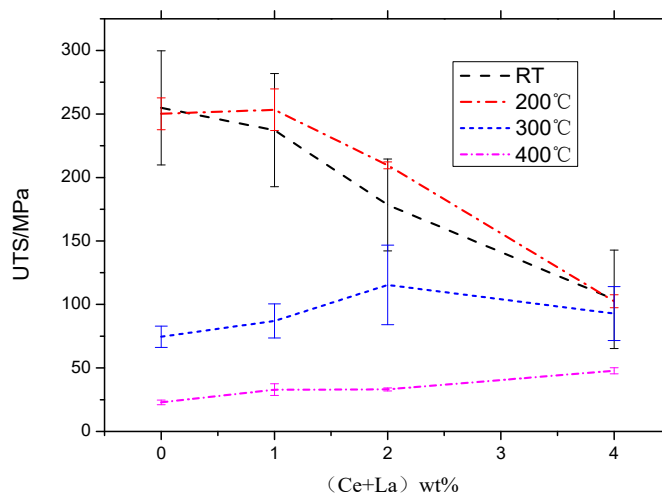


**Figure 7.** Ultimate Tensile Strength (UTS) from the tensile tests as a function of the (Ce and La) additions.

At room temperature, the  $\text{Al}_{11}(\text{Ce, La})_3$  is not having a positive contribution to tensile strength; usually, the UTS decreased with the temperature improve, but with the addition of 1% (Ce and La) or 2% (Ce and La), the tensile strength at 200 °C is even better than that at room temperature. At 300 °C, the addition of 2% (Ce and La) in the alloy increases the UTS strength by over 54.6% from 74.6 MPa to about 115.36 MPa compared with none (Ce and La) addition. Figure 6b,c shows the phases dispersed in the matrix, the smaller size phases precipitate, and the absence of cracks in the particles at lower (Ce and La) additions. The load-bearing theory plays an important ruler in the improvement of strength, which means stress could distribute at the intermetallic interface and improved stress distribution. Table 4 shows that the tensile strength of EN AC 46000 is 110 MPa and 20 MPa at 300 °C, 400 °C, respectively. The tensile strength of A3 alloys (2% Ce and La) at 300 °C and 400 °C is high than that of the EN AC 46000 alloy. The  $\text{Al}_{11}(\text{Ce, La})_3$  phases appear to form a network structure, and the structure is stable at elevated temperature, which may improve the high-temperature property.

At 400 °C, the addition of 4% (Ce and La) in the alloy, the UTS strength increased from 22.89 MPa to 47.82 MPa over 108.9% compared with none (Ce and La) addition. Although the large plate-like morphology of the primary precipitated  $\text{Al}_{11}(\text{Ce, La})_3$  phase harms the room temperature property, due to the high-temperature stable phases that could distribute stress, the 400 °C strength improved.

### 3.4. Modeling Particle Contribution to the Strength

As we know, with the increase of temperature, the alloy matrix begins to soften. Material thermal softening is mainly related to precipitation hardening and solution hardening, as well as the Peierls–Nabarro stress. The Peierls–Nabarro stress is called lattice friction which is baseline resistance to dislocation motion with a thermal component related to the Shear modulus that has a temperature dependence. The precipitates, such as  $\text{Mg}_2\text{Si}$  and  $\text{Al}_2\text{Cu}$ , prevent dislocation movement but may dissolve at elevated temperature, so there will be a balance between the precipitation hardening contribution and solution hardening. The additions of Cu, Mg and Si are not changed, and as a first approach, these are assumed unaffected by the additions of Ce+La. In the current approach, the RE free material is taken as a baseline, and these effects were in the modeling work attributed for in Equation (1) in the term  $\sigma_0$ . Treating the second phase particles resulting from the (Ce and La) additions in a similar manner as a reinforcing phase in a metal matrix composite, the strength can be

divided into the contribution from the base metal and the reinforcing particles. Following the treatment in Ceschini et al. [6].

$$\sigma = \sigma_0 + \Delta\sigma_{LB} + \Delta\sigma_{CTE} + \Delta\sigma_{MM} \quad (1)$$

where  $\sigma_0$  is the flow stress of the base alloy and  $\Delta\sigma_{LB}$  is the contribution from the load-bearing effect from the phases precipitated when adding (Ce and La) to the base material,  $\Delta\sigma_{CTE}$  is the strengthening from the dislocation generation during processing as a consequence of the thermal expansion mismatch. The last contribution is  $\Delta\sigma_{MM}$  is that from elastic modulus mismatch between the matrix and the particle and that will not affect the actual yield point but will affect the hardening of the material. As such, it will also influence the tensile strength. Any strengthening related to Orowan mechanisms will be neglected as these are only effective for small particles and, as such, will not have any significant contribution to the current set of particles. Similarly, as the secondary dendrite arm spacing had little influence, the Hall–Petch contribution should be seen as constant and included in the base material strength contribution.

Modeling will be based on the material without the (Ce and La) additions, and both yield strength and tensile strength, and elongation will be used as a baseline. The data used are collated in Table 4. As the phase properties are ill-determined, the yield strength, tensile strength, and elongation data will be used in an optimization process. The equations describing the strength contributions for load-bearing,  $\Delta\sigma_{LB}$ , coefficient of thermal expansion mismatch,  $\Delta\sigma_{CTE}$  and Modulus mismatch,  $\Delta\sigma_{MM}$ , according to Ceschini et al. [6] are written as:

$$\Delta\sigma_{LB} = 0.5\sigma_{ym}f_p \approx 0.5\sigma_0f_p \quad (2)$$

$$\Delta\sigma_{CTE} = \sqrt{3}\beta G_m b \sqrt{\frac{12f_p \Delta\alpha (T_p - T_u)}{bd_p}} \approx C_{CTE} \sqrt{\frac{f_p \Delta\alpha (T_p - T_u)}{d_p}} \quad (3)$$

$$\Delta\sigma_{MM} = \sqrt{3}\beta G_m b \sqrt{\frac{6f_p}{bd_p} \varepsilon} \approx C_{MM} \sqrt{\frac{f_p}{d_p} \varepsilon} \quad (4)$$

Here  $\sigma_{ym}$  is the matrix material yield point,  $f_p$  is the volume fraction particles,  $\beta$  is a constant, typically 0.5,  $G_m$  is the shear modulus,  $b$  is the Burgers vector,  $\Delta\alpha$  is the difference in thermal expansion coefficient between the particles and the matrix phase,  $T_p$  is the reference temperature at which stress starts to build up at the particle/matrix interphase,  $T_u$  is the use of test temperature,  $d_p$  is the characteristic particle size and  $\varepsilon$  is the plastic strain (here assumed zero at the yield point and identical to the elongation to failure at fracture)

The modeling was then made using the tensile data for alloy A1 at the different temperatures to give  $\sigma_0$  the appropriate temperature dependence. To get the values of  $C_{CTE}$ ,  $T_p$  and  $C_{MM}$  a nonlinear optimization process was used using Excel. Based on the microstructural observation of the significant difference of alloy A4 with the large particles, the data for the room temperature and 200 °C tests were omitted in the valuation. Base on the strong stress concentrations, the tensile and elongation data were also omitted at 300 °C and 400 °C for the same region. However, the yield strength at the two highest test temperatures was included as the results were deemed fit and that the stress concentration did not significantly alter the material performance.

The resulting parameters are collated in Table 5. Several different tests were made to ensure that the results were stable. In all cases, the contribution from thermal expansion mismatch ended up being zero, and this can only be interpreted as the actual thermal expansion between the  $Al_{11}(Ce, La)_3$  intermetallics and that of the Al matrix is small and negligible. The reference temperature for this would vary slightly in the optimizations but would typically end up in a stable solution near or below the solidus temperature of the alloy, and the chosen end-result was 477 °C. Given that the thermal expansion did not

contribute significantly, this should be seen as an uncertain value but still within what would be regarded as reasonable and expected. The last parameters were the modulus mismatch factor,  $C_{MM}$ . This was given a number greater than zero and, as such, affected strain hardening. This concluded that the strengthening effects seen from the (Ce and La) additions with the formation of the  $Al_{11}(Ce, La)_3$  intermetallics are primarily load-bearing to contribute to yield strengths and a modulus mismatch effect increasing the strain hardening rate of the composite. The quality of the fit as predicted vs. actual is shown in Figure 8. The red points included were not used in the fitting.

**Table 5.** Optimization parameters.

Parameter	RT	Yield Strength/YS (MPa)		
		200 °C	300 °C	400 °C
$\sigma_0$	196.39	161	59.2	19.19
$C_{CTE}$			0	
$T_p$			477	
$C_{MM}$			1.47	

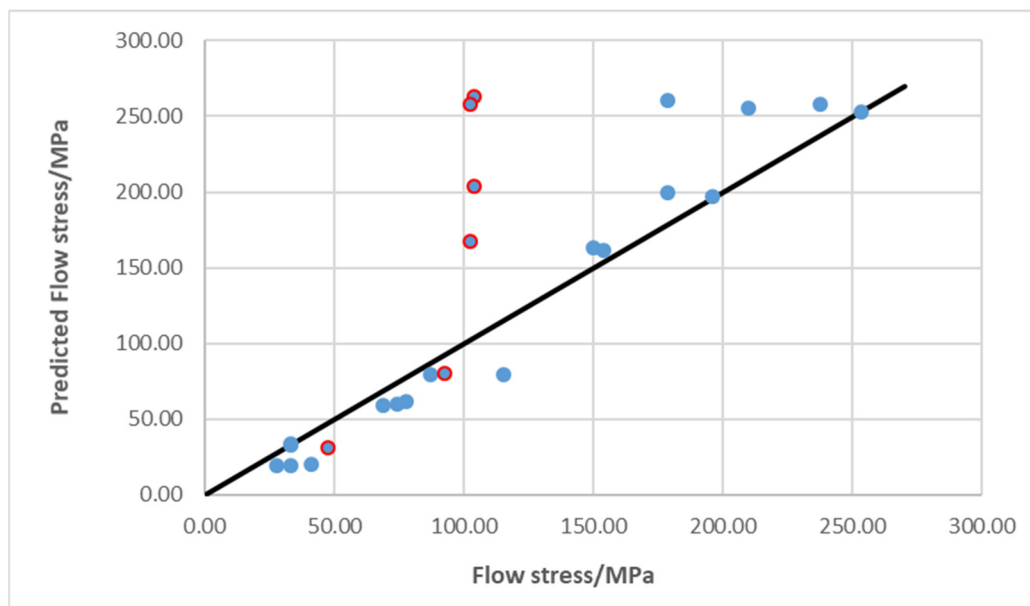


**Figure 8.** Model fit to experimental data showing the flow stress from the model prediction, Equations (1–4) versus the experimentally obtained flow stress. The red points are the data omitted in the fitting due to the brittle behavior.

#### 4. Conclusions

In the current study, the aim was to investigate the effect of (Ce and La) element additions, and then especially Ce and La additions on the room temperature and high-temperature mechanical properties. The base materials were four experimental Al-based alloys derived from an EN-AC 46000, adapted for squeeze casting with varying Ce and La additions. The following conclusions can be made

1. Squeeze-casting could be used to produce a sound material for all compositions
2. (Ce and La) addition primarily resulted in the precipitation of  $Al_{11}(Ce, La)_3$  and a possible modification of the  $\alpha-Al_{15}(Fe, Mn)_3Si_2$ , as Chinese script precipitates were absent.
3.  $Al_{11}(Ce, La)_3$  precipitated, as a primary precipitate, in small amounts at 2% (Ce and La) additions. At 4% (Ce and La) addition, a fully developed coarse primary precipitated plate-like  $Al_{11}(Ce, La)_3$  formed.

4. (Ce and La) additions did affect the mechanical properties due to the precipitation of  $Al_{11}(Ce, La)_3$  phase.
  - a. At room temperature, the UTS significantly drop with the additions of (Ce and La). The 4% RE addition showed the biggest drop of 59% strength compared with the material without RE addition. This drop was due to the cracks formed in the coarse primary  $Al_{11}(Ce, La)_3$  phases; the stress concentration was arising from the high aspect ratio plate-like phases;
  - b. At 200 °C, the 1% (Ce and La) additions showed the highest UTS. The improvement at 200 °C was 6.7% compared to the material without RE addition. The reason for the improvement was the smaller size precipitates carry part of the load without causing detrimental stress concentrations;
  - c. At 300 °C, the 2% (Ce and La) additions showed the highest UTS (115.36 MPa), which is a 54.63% strength improvement compared to the RE-free material. A network structure of  $Al_{11}(Ce, La)_3$  appears, that through a distributed load-bearing effect improved the high-temperature strength;
  - d. At 400 °C, the 4% (Ce and La) additions showed the highest UTS 47.82 MPa, which is a 108.91% strength-improvement compared with RE-free addition. Although the large plate-like morphology of the primary precipitated  $Al_{11}(Ce, La)_3$  phase significantly hampers the room temperature UTS, the high-temperature stable phases could carry the load and improve the high-temperature strength.
5. Through the modeling analysis, the nature of the strengthening mechanisms revealed that the dominant contribution to yield strength was the load-bearing mechanism.
6. Similarly, elastic modulus mismatch contributed to hardening and thus also kept the tensile strength high (UTS).

There was no contribution from thermal expansion mismatch to be resolved from the modeling, suggesting that the thermal expansion of  $Al_{11}(Ce, La)_3$  is similar to that of the aluminum alloy.

**Author Contributions:** Conceptualization, J.Z. and G.Y. and K.W.; formal analysis, A.E.W.J.; investigation, A.D.; resources, J.Z.; writing—original draft preparation, A.D.; writing—review and editing, A.D.; supervision, A.E.W.J.; project administration, G.Y. All authors have read and agreed to the published version of the manuscript.

**Funding:** This research was funded by the 1000 Foreign Expert Program from the Chinese government.

**Institutional Review Board Statement:** “Not applicable” for studies not involving humans or animals.

**Informed Consent Statement:** Informed consent was obtained from all subjects involved in the study.

**Data Availability Statement:** Data available in a publicly accessible repository.

**Conflicts of Interest:** The authors declare no conflict of interest. The funders had no role in the design of the study, in the collection, analyses, or interpretation of data, in the writing of the manuscript, or in the decision to publish the results.

## References

1. Kenworthy, J.R. Transport energy use and greenhouse gases in urban passenger transport systems: A study of 84 global cities. In Proceedings of the International Sustainability Conference, Fremantle, Australia, 17–19 September 2003; pp. 17–19. Available online: <http://researchrepository.murdoch.edu.au/21463/> (accessed on 19 September 2003).
2. Serrenho, A.C.; Norman, J.B.; Allwood, J.M. The impact of reducing car weight on global emissions: The future fleet in Great Britain. *Philos. Trans. R. Soc. A Math. Phys. Eng. Sci.* **2017**, *375*. [[CrossRef](#)] [[PubMed](#)]
3. Samuel, A. Developing Material Requirements for Automotive Brake Disc. *Mod. Concepts Mater. Sci.* **2019**, *2*. [[CrossRef](#)]

4. Kumar, J.; Singh, D.; Kalsi, N.S.; Sharma, S.; Pruncu, C.I.; Pimenov, D.Y.; Rao, K.V.; Kapłonek, W. Comparative study on the mechanical, tribological, morphological and structural properties of vortex casting processed, Al–SiC–Cr hybrid metal matrix composites for high strength wear-resistant applications: Fabrication and characterisations. *J. Mater. Res. Technol.* **2020**, *9*, 13607–13615. [[CrossRef](#)]
5. Samuel, A.; Ab, C.F. *Simulation Study on the Thermomechanical Behaviour of Al-Mc Automotive Brake Discs*; Eurobrake: Dresden, Germany, 2019; pp. 1–12.
6. Dieter, G.E.; Bacon, D.J. *Mechanical Metallurgy*; McGraw-Hill: New York, NY, USA, 1986; Volume 3, pp. 184–241.
7. Ceschini, L.; Dahle, A.; Gupta, M.; Jarfors, A.E.W.; Jayalakshmi, S.; Morri, A.; Rotundo, F.; Toschi, S.; Singh, R.A. Chapter 1, Metal Matrix Nanocomposites: An Overview. In *Aluminum and Magnesium Metal Matrix Nanocomposites*; Springer: Berlin, Germany, 2017; pp. 1–17.
8. Shaha, S.K.; Czerwinski, F.; Kasprzak, W.; Friedman, J.; Chen, D.L. Ageing characteristics and high-temperature tensile properties of Al–Si–Cu–Mg alloys with micro-additions of Mo and Mn. *Mater. Sci. Eng. A* **2017**, *684*, 726–736. [[CrossRef](#)]
9. Farkoosh, A.R.; Chen, X.G.; Pekguleryuz, M. Dispersoid strengthening of a high temperature Al–Si–Cu–Mg alloy via Mo addition. *Mater. Sci. Eng. A* **2015**, *620*, 181–189. [[CrossRef](#)]
10. Gaetke, L.M.; Chow-Johnson, H.S.; Chow, C.K. Copper: Toxicological relevance and mechanisms. *Arch. Toxicol.* **2014**, *88*, 1929–1938. [[CrossRef](#)] [[PubMed](#)]
11. Bjurenstedt, A.; Seifeddine, S.; Jarfors, A.E.W. The effects of Fe-particles on the tensile properties of Al–Si–Cu alloys. *Metals* **2016**, *6*, 314. [[CrossRef](#)]
12. Stadler, F.; Antrekowitsch, H.; Fragner, W.; Kaufmann, H.; Uggowitz, P.J. Effect of main alloying elements on strength of Al–Si foundry alloys at elevated temperatures. *Int. J. Cast Met. Res.* **2012**, *25*, 215–224. [[CrossRef](#)]
13. Lee, J.A. Cast aluminum alloy for high temperature applications. In Proceedings of the 132nd TMS Annual Meeting & Exhibition, San Diego, CA, USA, 2–6 March 2003; Volume 1, pp. 145–151.
14. Bogdanoff, T.; Dahle, A.K.; Seifeddine, S. Effect of Co and Ni Addition on the Microstructure and Mechanical Properties at Room and Elevated Temperature of an Al–7%Si Alloy. *Int. J. Met.* **2017**, *12*, 434–440. [[CrossRef](#)]
15. Stadler, F.; Antrekowitsch, H.; Fragner, W.; Kaufmann, H.; Uggowitz, P.J. The effect of Ni on the high-temperature strength of Al–Si cast alloys. In *Materials Science Forum*; Trans tech Publications: Switzerland, 2011; Volume 690, pp. 274–277. [[CrossRef](#)]
16. Feng, J.; Ye, B.; Zuo, L.; Qi, R.; Wang, Q.; Jiang, H.; Huang, R.; Ding, W. Effects of Ni content on low cycle fatigue and mechanical properties of Al–12Si–0.9Cu–0.8Mg–xNi at 350 °C. *Mater. Sci. Eng. A* **2017**, *706*, 27–37. [[CrossRef](#)]
17. Song, M.; Xiao, D.; Zhang, F. Effect of Ce on the thermal stability of the  $\Omega$  phase in an Al–Cu–Mg–Ag alloy. *Rare Met.* **2009**, *28*, 156–159. [[CrossRef](#)]
18. Liao, H.C.; Xu, H.T.; Hu, Y.Y. Effect of RE addition on solidification process and high-temperature strength of Al–12%Si–4%Cu–1.6%Mn heat-resistant alloy. *Trans. Nonferrous Met. Soc. China* **2019**, *29*, 1117–1126. [[CrossRef](#)]
19. SAwe, A.; Seifeddine, S.; Jarfors, A.E.W.; Lee, Y.C.; Dahle, A.K. Development of new Al–Cu–Si alloys for high temperature performance. *Adv. Mater. Lett.* **2017**, *8*, 695–701. [[CrossRef](#)]
20. Anderson, K.; Weritz, J.; Kaufman, J.G. 360.0 and A360.0\*. In *Properties and Selection of Aluminum Alloys*; ASM International: Almere, The Netherlands, 2019; Volume 2B, pp. 558–559.
21. Anderson, K.; Weritz, J.; Kaufman, J.G. 359.0\*. In *Properties and Selection of Aluminum Alloys*; ASM International: Almere, The Netherlands, 2019; Volume 2B, pp. 556–557.
22. Anderson, K.; Weritz, J.; Kaufman, J.G. 319.0, A319.0, B319.0, and 320.0\*. In *Properties and Selection of Aluminum Alloys*; ASM International: Almere, The Netherlands, 2019; Volume 2B, pp. 533–535.
23. Anderson, K.; Weritz, J.; Kaufman, J.G. 332.0. In *Properties and Selection of Aluminum Alloys*; ASM International: Almere, The Netherlands, 2019; Volume 2B, pp. 536–537.
24. Anderson, K.; Weritz, J.; Kaufman, J.G. 354.0. In *Properties and Selection of Aluminum Alloys*; ASM International: Almere, The Netherlands, 2019; Volume 2B, pp. 542–543.
25. Anderson, K.; Weritz, J.; Kaufman, J.G. 355.0 and C355.0\*. In *Properties and Selection of Aluminum Alloys*; ASM International: Almere, The Netherlands, 2019; Volume 2B, pp. 544–547.
26. Anderson, K.; Weritz, J.; Kaufman, J.G. 356.0 and A356.08\*. In *Properties and Selection of Aluminum Alloys*; ASM International: Almere, The Netherlands, 2019; Volume 2B, pp. 548–552.
27. Anderson, K.; Weritz, J.; Kaufman, J.G. 357.0 and Variations A357.0 to F357.0\*. In *Properties and Selection of Aluminum Alloys*; ASM International: Almere, The Netherlands, 2019; Volume 2B, pp. 553–555.
28. Gariboldi, E.; Lemke, J.N.; Ozhoga-Maslovskaja, O.; Timelli, G.; Bonollo, F. High temperature behaviour of 46000, 46100, 47100 Al die cast parts. *Metall. Ital.* **2016**, *108*, 13–16.
29. Chang, J.; Moon, I. Refinement of cast microstructure of hypereutectic Al–Si alloys through the addition of rare earth metals. *J. Mater. Sci.* **1998**, *3*, 5015–5023. [[CrossRef](#)]
30. Ghassemali, E.; Riestra, M.; Bogdanoff, T.; Kumar, B.S.; Seifeddine, S. Hall-Petch equation in a hypoeutectic Al–Si cast alloy: Grain size vs. secondary dendrite arm spacing. *Procedia Eng.* **2017**, *207*, 19–24. [[CrossRef](#)]
31. Kai, W. Introduction of 2002 Edition National Standard of Metallic Materials—Brinell Hardness Test. *Heat Treat. Met. China* **2006**, *2002*, 101–103.

32. Du, Y.; He, C.; Schuster, J.C.; Liu, S.; Xu, H. Thermodynamic description of the Ni-Si-Ti ternary system. *Int. J. Mater. Res.* **2006**, *97*, 543–555. [[CrossRef](#)]
33. Fan, C.; Long, S.Y.; de Yang, H.; Wang, X.J.; Zhang, J.C. Influence of Ce and Mn addition on  $\alpha$ -Fe morphology in recycled Al-Si alloy ingots. *Int. J. Miner. Metall. Mater.* **2013**, *20*, 890–895. [[CrossRef](#)]
34. Baldan, R.; Malavazi, J.; Couto, A.A. Microstructure and mechanical behavior of Al9Si0.8Fe alloy with different Mn contents. *Mater. Sci. Technol.* **2017**, *33*, 1192–1199. [[CrossRef](#)]
35. Elgallad, E.M.; Ibrahim, M.F.; Doty, H.W.; Samuel, F.H. Microstructural characterisation of Al-Si cast alloys containing rare earth additions. *Philos. Mag.* **2018**, *98*, 1337–1359. [[CrossRef](#)]
36. Aghaie, E. Effect of Cerium Addition on Improvement of Mechanical Properties of B319 Powertrain Aluminum Alloy. Ph.D. Thesis, University of British Columbia, Vancouver, BC, Canada, 2019; p. 130.